RESEARCH ARTICLE

NANO · MICRO small
www.small-journal.com

Gray-Level Guided Image-Activated Droplet Sorter for Label-Free, High-Accuracy Screening of Single-Cell on Demand

*Zhen Liu, Yidi Zhang, Jianing Li, Shuxun Chen, Han Zhao, Xin Zhao, and Dong Sun**

Single-cell encapsulation in droplet microfluidics has become a powerful tool in precision medicine, single-cell analysis, and immunotherapy. However, droplet generation with a single-cell encapsulation is a random process, which also results in a large number of empty and multi-cell droplets. Current microfluidics sorting technologies suffer from drawbacks such as fluorescent labeling, inability to remove multi-cell droplets, or low throughput. This paper presents a gray-level guided image-activated droplet sorter (GL-IADS), which enables label-free, high-accuracy screening of single-cell droplets by rejecting empty and multi-cell droplets. The gray-level based recognition method can accurately classify droplet images (empty, single-cell, and multi-cell droplets), especially in differentiating empty and cell-laden droplets (accuracy of 100%). Crucially, this method reduces the image processing time to ≈300 µs, which makes the GL-IADS possible to reach an ultra-high sorting throughput up to hundreds or even KHz. The GL-IADS integrates the novel recognition method with a detachable acoustofluidic system, achieving sorting purity of 97.9%, 97.4%, and >99% for single-cell, multi-cell, and cell-laden droplets, respectively, with a throughput of 43 Hz. The GL-IADS holds promise for numerous biological applications that are previously difficult with fluorescence-based technologies.

1. Introduction

Deciphering population heterogeneity is of great interest in cellular biology.[1–3] Conventional biological studies for cell analysis often rely on cell populations, which can ensure the average properties of detection substance but fail to capture the heterogeneity between populations.[4,5] Recent efforts have increasingly recognized the significance of single-cell studies in biomedical fields.[6,7] The existing technologies for single-cell analysis include flow cytometry,[8] fluorescence-activated cell sorting (FACS),[9] image-activated cell sorter (IACS),[10] manual micromanipulation,[9] micropore array,[11] and droplet microfluidics[12]. Flow cytometry is regarded as the gold standard in biological laboratories. Nevertheless, the high instrument price and the cell damage risk due to high voltage make it not so ideal for single-cell analysis.[13] FACS is an indispensable tool owing to its high-throughput, but it also decreases cell activity due to the stress exerted on the cells.[14] IACS can identify multiple cell types in a label-free manner based on machine learning.[15] Yet, the long image processing time and high requirements for advanced imaging hardware is a big challenge in achieving high sorting throughput.[16] Manual micromanipulation allows for gentle handling of cells, but it is generally inefficient.[17] Micropore array can achieve single-cell capture and maintain the cell viability. This technology, combined with some recognition technologies such as laser-induced forward transfer,[18,19] can achieve high-accuracy single-cell sorting. However, the micropore size must be precisely matched to the target cell size, and its throughput of 1000 h is still much lower than that of FACS. The droplet microfluidics platform has become an powerful tool for high-throughput single-cell analysis,[20,21] drug screening,[22,23] and diagnosis of diseases.[24,25] The isolated droplet provides an independent microenvironment to study the protein secretion, enzyme activity, and proliferation of individual cells. It also reduces cross-contamination and maintains cell activity at the single-cell level. Compartmentalization of single-cell into each individual water-in-oil microdroplets has revolutionized genomics, transcriptomics, and proteomics research.[4,26]

Z. Liu, Y. Zhang, J. Li, S. Chen, H. Zhao, D. Sun
Department of Biomedical Engineering
City University of Hong Kong
Hong Kong SAR, China
E-mail: medsun@cityu.edu.hk

Y. Zhang, X. Zhao
National Key Laboratory of Intelligent Tracking and Forecasting for Infectious Diseases
Engineering Research Center of Trusted Behavior Intelligence
Ministry of Education
Tianjin Key Laboratory of Intelligent Robotic (tjKLIR)
Institute of Robotics and Automatic Information System (IRAIS)
Nankai University
Tianjin 300350, China

X. Zhao
Institute of Intelligence Technology and Robotic Systems
Shenzhen Research Institute of Nankai University
Shenzhen 518083, China

The ORCID identification number(s) for the author(s) of this article can be found under https://doi.org/10.1002/smll.202500520

DOI: 10.1002/smll.202500520

Despite the great advantages of droplet microfluidics for single-cell studies, cell quantity encapsulated in droplets is dominated by Poisson distribution.[27] To minimize the proportion of multi-cell droplets, a low-concentration of cell suspensions for droplet encapsulation is required, but it also results in a low encapsulation rate of single cells (<5%) and a majority of empty droplets.[28] The large number of empty droplets make the downstream process difficult and time-consuming. Therefore, a microfluidics platform that can sort single-cell droplets is required. To date, the most commonly used technology for single-cell droplet sorting is fluorescence-activated droplet sorter (FADS).[29–31] This technology makes sorting decision depending on photo counts from the encapsulated cells labeled by fluorescence biomarkers.[14] However, although FADS can achieve reliable droplet separation, it has several critical drawbacks. First, labelling these biomarkers can possibly alter the properties of the original cells or damage cells, causing the sorted cells to not show the same characteristics as the original cells and thus cannot be used for subsequent biological analysis.[16,32,33] In particular, many cell types cannot be high-specificity fluorescently labeled, or they even have no biomarkers.[34,35] Second, FADS cannot distinguish the quantity of cells encapsulated in a droplet, which results in it being unable to remove multi-cells droplets.[36] To achieve high-purity screening of single-cell droplets, FADS has to adopt low-concentration cell encapsulation to avoid the presence of multi-cell droplets.[23,37] However, the rising number of empty droplets and the low proportion of single-cell droplets acts to lower sorting throughput, showing a trade-off relationship between the purity and throughput in single-cell droplet sorting. These shortcomings limit the application of FADS in single-cell studies.

Imaging-based approaches are becoming increasingly popular in droplet sorting studies, especially with the development of image processing algorithms, interface speeds and processing hardware in recent years.[38,39] High-resolution images enable real-time visual recognition of droplets, which can be coupled with droplet sorting without the use of label reagent. Indeed, machine learning strategies, such as templated matching,[40] convolutional neural networks (CNNs),[39] "You Only Look Once" (YOLO),[41] and other deep learning-based detection models,[2,28,42] have been implemented in cell-laden droplet sorting. This technology can identify the cell quantity encapsulated in droplet, which makes it possible to achieve single-cell droplets sorting regardless of the probability of multi-cell droplets. However, the applications of machine learning techniques to high-throughput image-activated droplet sorter (IADS) have proven to be a big challenge due to the long image processing time and high requirements for imaging and GPU hardware.[16,41] In IADS technologies, completing a target object sorting needs image acquisition, image processing (object detection, classification and decision-making), and actuation.[10,41]. Image acquisition can be completed in microseconds by using a high-speed camera.[43] Actuation methods, such as acoustofluidics[23,37] and dielectrophoresis[14], can meet the droplet sorting throughput requirement up to several kHz. However, image processing is the most time-consuming part. It needs high computational power to evaluate millions of learned parameters on the real-time image processor, resulting in the image processing time of at least dozens of milliseconds.[16,44] The long image processing time caused the sorting throughput of even state-of-the-art IADS to be 100 times lower than that of FADS,[12,39,41] which is difficult to meet the requirements for conducting population-scale biological experiments.

In this article, we present a gray-level guided image-activated droplet sorter (GL-IADS), which enables label-free, high-accuracy screening of single-cell droplets, multi-cell droplets, and both (cell-laden droplets) on demand. The gray-level based recognition method can accurately classify droplets into empty, single-cell, and multi-cell according to the cell quantity encapsulated in the droplet. In particular, the accuracy of distinguishing empty and cell-laden droplets reaches 100%. The recognition capability enables the sorter to sort single-cell droplets by rejecting empty and multi-cell droplets from a high-concentration cell encapsulation, overcoming the aforementioned trade-off. Moreover, the recognition methods shorten the image processing time (droplet detection, classification, and decision-making) to ≈300 µs, which makes the GL-IADS possible to reach an ultra-high sorting throughput up to hundreds or even KHz. [41,42,44] Yet it does not require high-performance computing computers. For the acoustofluidic actuation system, the disposable polydimethylsiloxane (PDMS) channel can be reversibly coupled and detached from the expensive surface acoustic wave (SAW) transducer to avoid biological contamination. A designed micropillar reduced acoustic energy attenuation to enable reliable droplet deflection. Finally, the GL-IADS achieved sorting purity of 97.9%, 97.4%, and >99% for single-cell, multi-cell, and cell-laden droplets, respectively, at a throughput of 43 droplets s^{-1}. The sorter also ensured the monodispersity of the sorted droplets by rejecting merged droplets and/or droplet debris. The high viability (>93%) of recovered cells demonstrates the biocompatibility of the sorter. The GL-IADS holds promise for numerous biological applications that are previously difficult with fluorescence-based sorting technologies.

2. Results

2.1. Schematic of the GL-IADS

The GL-IADS consists of two components: a detachable acoustofluidic system and an image detection module (**Figure 1A**). The detachable acoustofluidic system is specifically engineered for droplets loading, focusing and deflection. The arrangement of the device is shown in Figure 1B,C. The SAW transducer is fabricated by depositing a pair of unidirectional focus interdigital transducers (U-FIDTs) on a lithium niobate (LiNbO3) substrate. The disposable PDMS channel features two inlets, two outlets, and a sorting channel. The disposable PDMS channel and SAW transducer are physically coupled via a micropillar, which acts as a waveguide to transmit the acoustic energy from the SAW transducer into the sorting channel. The image detection module is designed for droplet imaging and recognition. A CMOS camera is used to acquire the sorting channel in real time, and then the image processing system detects, classifies, and makes a decision on the droplet by analyzing each acquired image. The image processing system could real-time classify droplets into empty, single-cell, and multi-cell

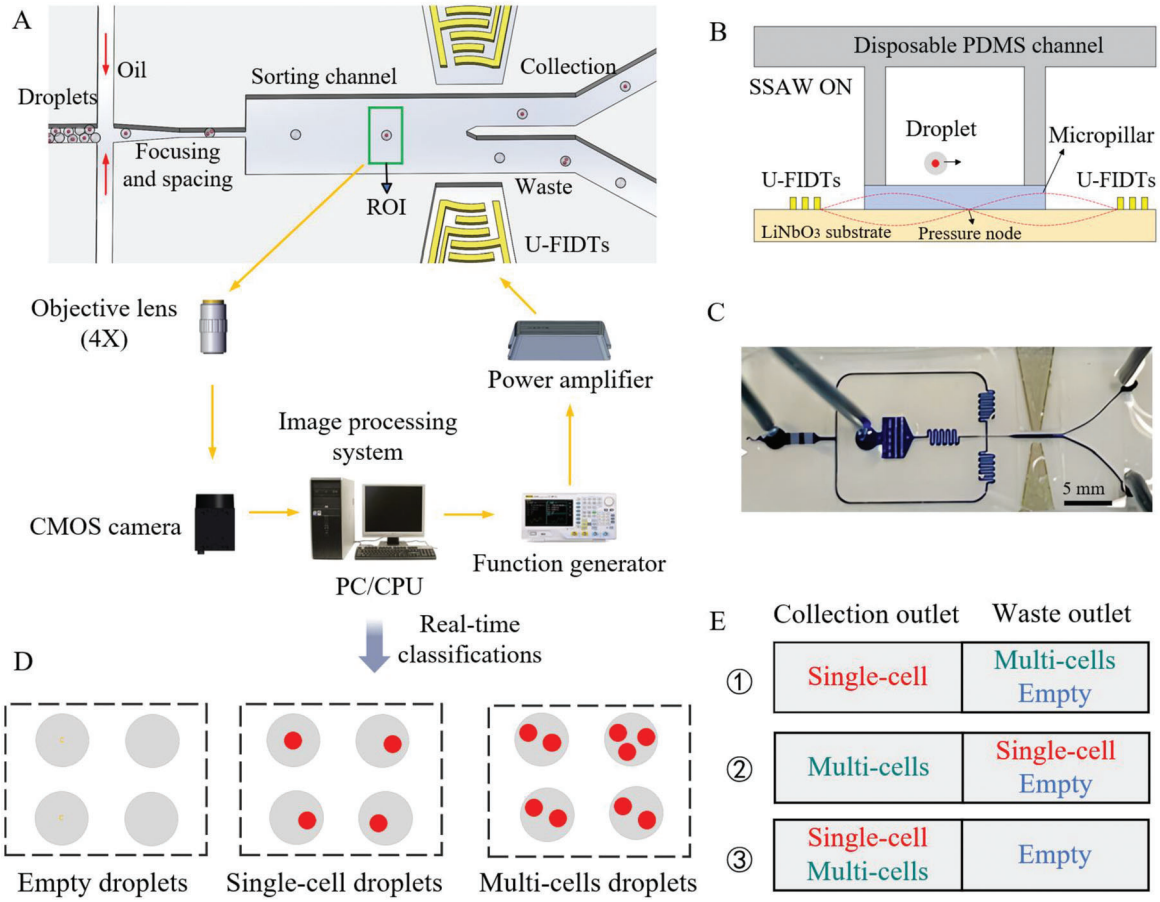

Figure 1. Overview of the GL-IADS. A) Experiment setup of GL-IADS and droplet sorting process. B) Illustration of droplet deflection in the detachable acoustofluidic system. C) Photograph of the detachable acoustofluidic system. D) Real-time droplet classification of empty, single-cell, and multi-cell. E) Selectable screening of droplets with various cell numbers.

based on the gray-level recognition method (Figure 1D). Based on this, the GL-IADS has three options for target droplet screening, including single-cell, multi-cell, and cell-laden droplets (Figure 1E).

The single-cell droplet sorting procedure is also illustrated in Figure 1A. Droplets and HEF-7500 oil were injected into the disposable PDMS channel from the middle and peripheral inlets, respectively. Under the action of the oil phase, the injected droplets were focused into a central straight streamline and maintained a certain distance between neighbors, ensuring each droplet had enough space for image detection and SAW deflection. In the sorting channel, a region of interest (ROI) of the image was set. All focused droplets would pass through the ROI one by one. Each droplet within the ROI could be classified in real time. When the single-cell droplet was detected, the image processing system gave the U-FIDTs a turn-on command to form a standing surface acoustic wave (SSAW) field. Under the action of acoustic radiation force (ARF), the detected single-cell droplet was drawn to the pressure node of SSAW and finally flowed into the collection outlet. The other non-target droplets maintained their route to flow into the waste outlet due to a low flow resistance.

2.2. Real-time Droplet Detection, Classification, and Decision-making

Here, we use class "0", class "1", and class ">1" to represent empty, single-cell, and multi-cell droplets, respectively. The microscopic images of the sorting channel were acquired at 320 frames per second (fps) and processed frame by frame. **Figure** 2A illustrates the process of droplet detection, classification, and decision-making. For each acquired microscopic image, the ROI was extracted and reconstructed to a new grayscale image with 8-bit pixel depth. Then, a Hough circle transform algorithm (Note S1, Supporting Information) was used to identify whether a droplet was present in the form of a circle. The radial detection parameter was set within the range from 13.5 to 14.5 pixels. It could identify the monodisperse droplets with a diameter of 45 μm without omission, which was also used to control the size uniformity of the sorted droplets by rejecting droplet debris and/or merged large droplets. Upon detecting a droplet, a square detection area, made up of a 19 × 19-pixel array with a total of 361 pixels, centered on the center of this circle, was established. Then, the image processing system began to scan and

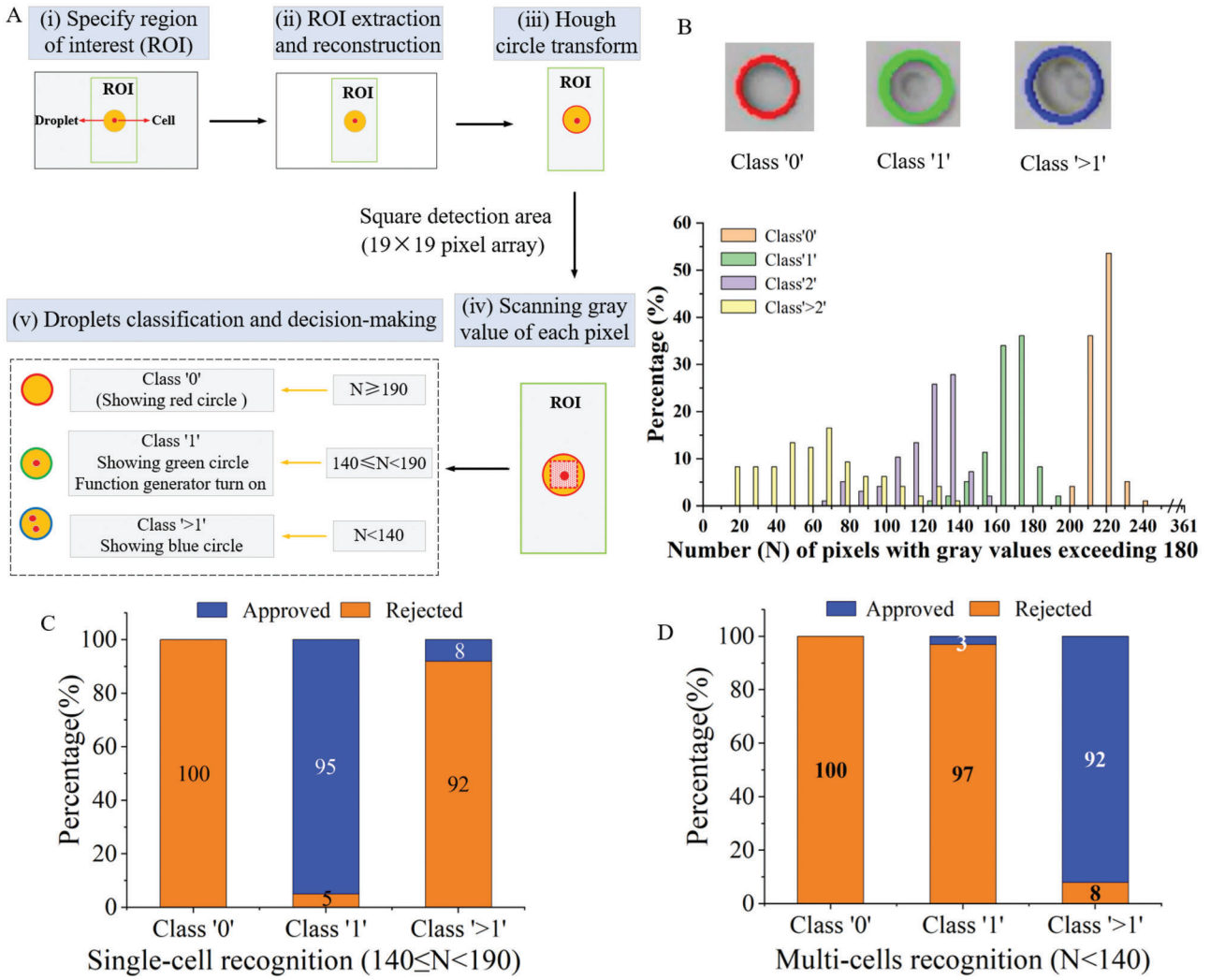

Figure 2. Principle of droplet detection, classification and decision-making. A) Image processing procedure. i) Each acquired live microscopic image has a ROI in the sorting region. ii) ROI was extracted and reconstructed to a grayscale image with 8-bit pixel depth. iii) A Hough circle transform algorithm was used to detect droplets in this ROI. iv) If a droplet was detected, a square area was created in circle (droplet), and then the image processing system scanned and counted the gray value of each pixel in this square area. v) The image processing system classified droplets and made a decision based on droplet classification parameter N. B) Droplet classification parameter. The total pixels number of square area is 361, of which the number (N) of pixels with gray value exceeding 180 determines droplet classification. C) Single-cell droplet recognition accuracy when 140 ≤ N < 190. D) Multi-cell droplet recognition accuracy when N < 140.

count the gray values (range of 0–255) of each pixel of this square area. Inside a droplet, the cell has a deeper color than water, and it appeared typically as a gray ball with a radius of ≈6 pixels. Therefore, the more cells in the square area, the fewer the pixels with high gray value. For each detected droplet image, a corresponding text file containing the gray value of 361 pixels (Figure S1, Supporting Information) was outputted. We analyzed 300 droplet images for class "0", "1", and ">1" (number of "2" was 260, ">2" was 40), respectively. The number (N) of pixels with gray value exceeding 180 in the square area has an obvious difference in the three droplet classifications, detail as the parameter graph in Figure 2B. The N of the class "0" population was all in the range of 200–250. The N of 95% class "1" population were in the range of 140–190, where 8% of the class "2" population were present. The N of 92% class "2" and 100% class ">2" population were below 140, where 3% of the class "1" population were present. No overlap was found between class "0" and class "1", indicating that the classification parameter N could completely distinguish empty with cell-laden droplets. The less overlap between class″1″ and class ">1" was mainly attributed to a few cells being very large and even reaching the sum of two cells size. According to the parameter graph, for the recognition of single-cell droplets, N in the range of 140–190 can reject 100% empty and 92% multi-cells, while losing 5% single-cell droplets (Figure 2C). For that of multi-cell droplets, the range below 140 can reject 100% empty and 97% single-cell, while losing 8% multi-cell droplets (Figure 2D). To show the recognition accuracy of the sorter, three colors of red, green, and blue were used to represent class "0", class "1", and class '>1″ respectively. In real-time single-cell droplet sorting,

when detecting class '1', the image processing system denoted this droplet in green color and simultaneously turned on SSAW for 200 µs. For the other two classifications, class '0" was denoted in red color, class '>1" in blue color, and the SSAW remained off. The average processing time for each microscopic image, including droplet detection, classification, and decision-making (Figure 2A), measured using a high-resolution clock from the C++ chrono library for 10 000 images, was ≈300 µs (recording as Figure S2, Supporting Information).

The robustness of the GL-IADS needs to be guaranteed. In the sorter, the exposure parameter and real-time image acquisition frame rate were fixed to avoid altering the appearance of moving droplets in the microchannel. However, the gray-level based droplet recognition method is very sensitive to the light intensity of the microscope, and the light intensity adjusted in each experiment cannot be exactly the same. To avoid repeated debugging for droplet classification parameters, a light intensity drift correction algorithm was adopted. First, the average pixels' gray value (G_1) of the ROI area was calculated in one sorting experiment. Second, a function was set on the basis of G_1: $G_{AN}(x, y) = G_N(x, y) + (G_1 - G_N)$, where G_N is the average pixel gray value of the rectangle area manually selected from ROI in the Nth experiment, $G_N(x, y)$ is the gray value of each pixel of ROI area in the Nth experiment, $G_{AN}(x, y)$ is the adjusted gray value of each pixel of ROI area in the Nth experiment. The Nth run of the sorting program represents Nth experiment. Each time running the sorting program, we just need manually select a rectangle area in ROI to adjust the gray value of each pixel of ROI then began the sorting experiment. The light intensity drift correction algorithm overcomes the light intensity influence of the microscope, ensuring stable droplet classification without changing the classification parameters every time.

2.3. Detachable Acoustofluidic System for Droplet Deflection

The disposable PDMS channel was assembled with an SAW transducer under the van der Waals force-induced self-adhesion. After each test, the disposable PDMS channel was peeled off and discarded, which avoided cross-contamination and kept the expensive SAW transducers reusable. The SAW transducer of U-FIDTs has been proved to have a much stronger transmission energy than straight IDTs and regular FIDTs because the acoustic amplitude propagating toward the focused center is larger than the reverse direction.[23,45] When the two U-FIDTs were applied with an AC signal, two series of identical SAWs were generated and propagated along the surface of the $LiNbO_3$ substrate toward the microchannel. The two traveling SAWs interfered with each other and formed the SSAW.[46,47] Such SSAW transmitted into the disposable PDMS channel through a micropillar, the droplets in the microchannel were deflected into the pressure nodal line under the effect of ARF.[45] In this chip, the pressure nodal line was designed to be 60 µm upward from the center of the sorting channel, which is sufficiently deflect all droplets into the collection outlet.

Due to the strong damping in PDMS, coupling the entire PDMS channel device to the SAW transducer by a PDMS film results in severe acoustic energy attenuation.[48] And the thicker this film is, the more energy is lost. Here, a designed PDMS micropillar was used to transfer acoustic energy from the LiNbO3 substrate into the PDMS channel. This micropillar covered the sorting channel while minimizing the contact area between U-FIDTs and the PDMS device to reduce wave attenuation. In contrast to other works [48,49] this fabrication of micropillars does not require photolithography on the film, which could reduce the thickness as soon as possible. Meanwhile, no complicated alignment issues occur between the sorting channel and the micropillar. A droplet deflection experiment was conducted to prove the advantage of the micropillar. Two disposable PDMS channels, bonding the top PDMS channel to a micropillar (micropillar-PDMS channel) and an untrimmed PDMS film (film-PDMS channel), respectively, were performed at the same SAW transducer (U-FIDTs). The thickness of the micropillar and untrimmed PDMS film was the same. All droplets flowed into the waste outlet at a flow rate of 370 µL min^{-1} when SSAW was turned off (**Figure 3A,B**). After inputting an AC signal with the resonance frequency of 9.73 MHz into U-FIDTs, the deflection distance of the droplets was recorded by a microscope (Figure 3D,E). The quantitative relationship of deflection distance versus input voltage in each chip is shown in Figure 3G. For the micropillar-PDMS channel, when the input power was 16 Vpp, the deflection distance of droplets reached 38 µm, which was enough to push all droplets into the collection outlet. After the input power was increased to 32 Vpp, the droplets reached the designed maximum distance of 60 µm. By contrast, for the film-PDMS channel, the maximum deflection distance of droplets was 18 µm, even in 40 Vpp, which could only deflect ≈40% of droplets into the collection outlet. The assay revealed that the micropillar-PDMS channel had a smaller acoustic attenuation than the film-PDMS channel. Another experiment comparing the energy transmission efficiency of U-FIDTs and regular FIDTs was conducted (Figure 3A,C,D,F). A same disposable micropillar-PDMS channel was performed in two SAW transducers (U-FIDTs and regular FIDTs). Under the resonance frequency (9.63 MHz) of regular FIDTs, the droplets were also deflected to collection outlet without omission. However, the regular FIDTs required 40 Vpp to achieve a maximum deflection distance of 55 µm, whereas U-FIDTs required only 24 Vpp (Figure 3H). The comparison result indicated that U-FIDTs had a stronger acoustic energy transmission efficiency. The detachable acoustofluidic chip assembled by U-FIDTs and micropillar-PDMS channel has high energy utilization, which make the GL-IADS more reliable to achieve target droplet sorting.

2.4. Performance of GL-IADS in Sorting Cell Quantity in Droplets

The performance of the GL-IADS was demonstrated by sorting single-cell droplets from a high-concentration cell encapsulation. The cell quantity encapsulated in the droplet was dominated by a Poisson distribution: $P(k) = \lambda^k e^{-\lambda}/k!$ where k is the number of cells in a droplet and λ is the average number of cells in per droplet.[27] **Figure 4E** shows the simulated possibility of a number of cells encapsulated in a droplet with different λ values from 0.1 to 0.9. Conventional droplet sorters adopt low-concentration cell encapsulation with λ less than 0.1 to reduce the proportion of multi-cell droplets. Here, to demonstrate our sorter could achieve high-accuracy screening of single-cell droplets regardless

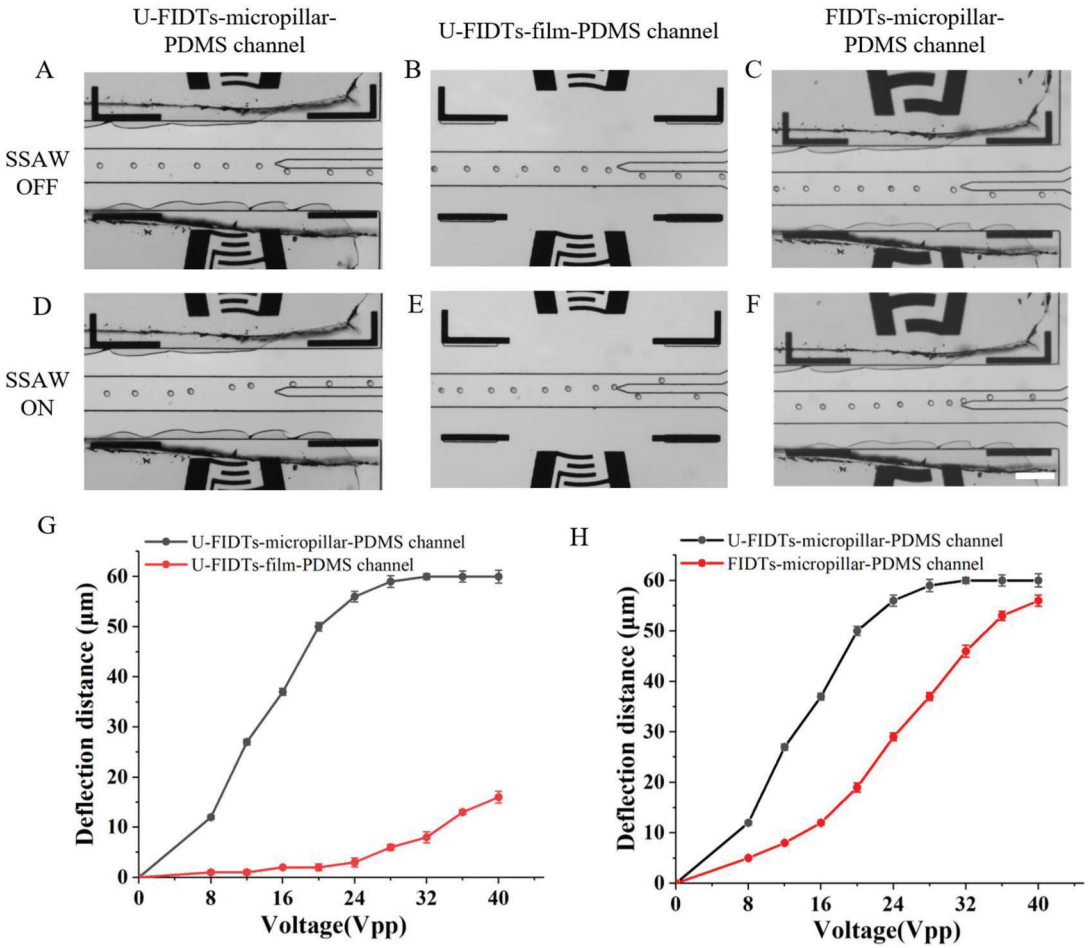

Figure 3. Performance of micropillar-PDMS channel and U-FIDTs in comparison with film-PDMS channel and regular FIDTs in acoustic energy utilization. Snapshots of droplet flow in U-FIDTs-micropillar-PDMS channel when SSAW was A) off and D) on. Snapshots of droplet flow in the U-FIDTs-film-PDMS channel when SSAW was B) off and E) on. Snapshots of droplet flow in regular FIDTs-micropillar-PDMS channel when SSAW was C) off and F) on. Scale bar: 200 μm. G) Comparison of droplet deflection distance versus input voltage in U-FIDTs-micropillar-PDMS channel and U-FIDTs-film-PDMS channel. H) Comparison of droplet deflection distance versus input voltage in U-FIDTs-micropillar-PDMS channel and regular FIDTs-micropillar-PDMS channel.

of the presence of multi-cell droplets, we adopted a cell encapsulation with λ of 0.7 to conduct this experiment. The cell line used for droplet encapsulation and sorting is human adipose-derived mesenchymal stem cells (ADSCs).

The droplet classification parameter of N for classes "0", "1", and ">1" were set to ≥190, 140–190, and <140, respectively. When a single-cell droplet was detected, the U-FIDT was input with an AC signal with an amplitude of 32 Vpp and resonant frequency of 9.73 MHz for 200 μs. Figure 4A shows the sorting process of a single-cell droplet. At 0 ms, a single-cell droplet entered the ROI and immediately displayed a green circle, indicating this droplet image has been acquired, detected, classification, and decision-making. At the same time, the function generator received the command to turn on. At 9.354 ms, the droplet entered the SSAW field and was drawn toward the collection outlet. At 21.826 ms, the droplet was about to enter the collection outlet, and an empty droplet entered the ROI. At 43.652 ms, the single-cell and empty droplet entered the collection and waste outlet respectively, and a new multi-cell droplet was detected in ROI. A video (Movie S1, Supporting Information) visually showed that the GL-IADS accurately recognized the three droplet classifications and sorted the single-cell droplets without mistake. Even the overlapping cells in the droplet could be successfully classified because their color is darker than individual cells. When performing droplet sorting, the distance of the adjacent droplets must be taken into account. In the GL-IADS, the latency time of the function generator switch, fully turned on and off after the sorting-signal trigger, was 12 ms. Therefore, the detection time interval of adjacent droplets in the ROI needs to exceed 12 ms to ensure only one droplet in the SSAW field for one separation. Otherwise, more than one droplet may be sorted at one time, or the function generator cannot be turned on in time for the next droplet sorting. In this work, a time interval limit of ≈23 ms between adjacent droplets was applied by precaution to prevent erroneous sorting, achieving a droplet sorting throughput of 43 per second.

The purity of sorted single-cell droplets was analyzed. Before sorting, ≈34.7% of droplets contained single-cell while 49.7% were empty droplets and 15.6% of droplets contained multi-cell (Figure 4B,E). After sorting, the purity of single-cell droplets

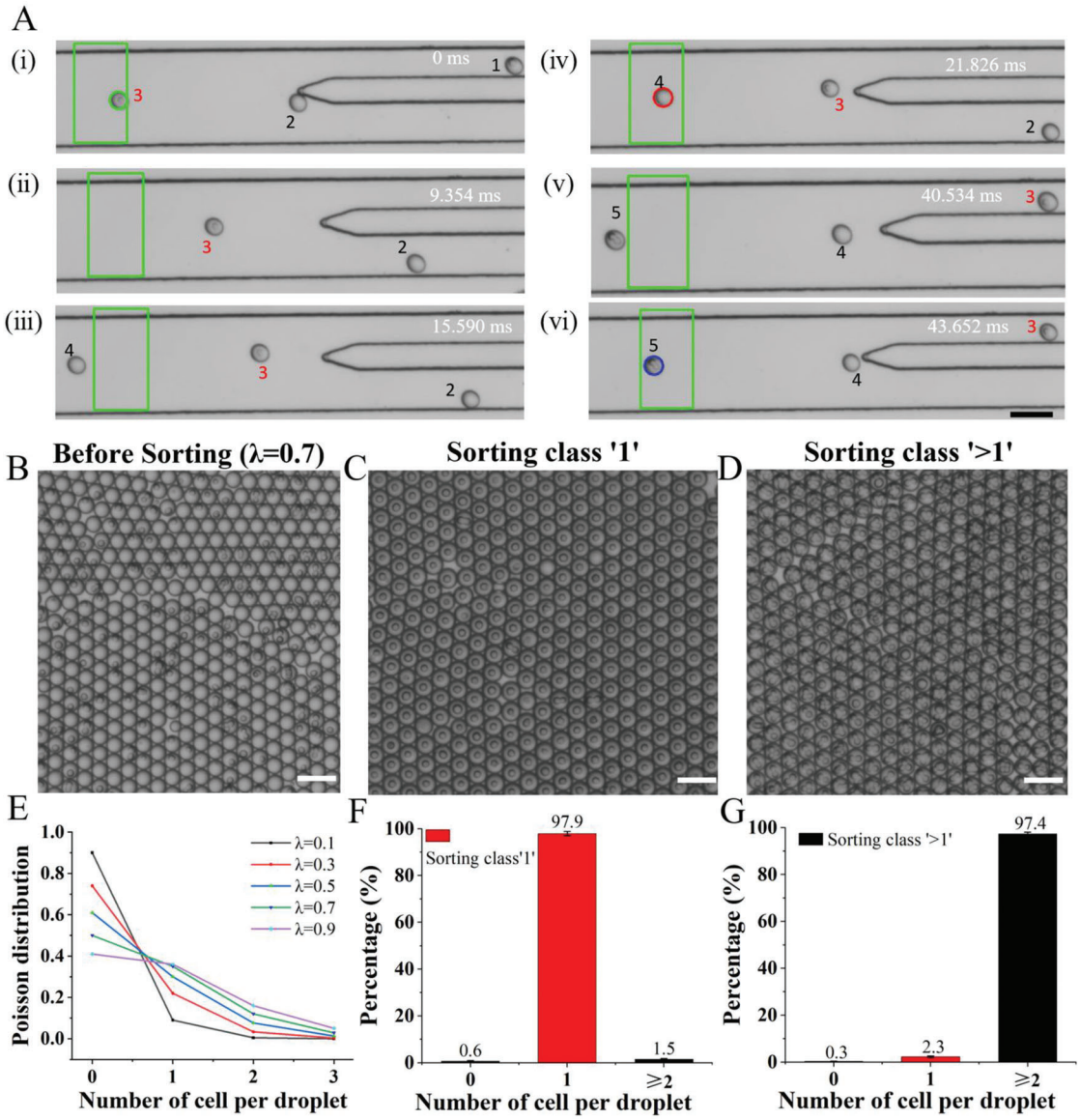

Figure 4. Performance of GL-IADS. A) A complete sorting process of single-cell droplet, recorded by a CMOS camera at 320 fps (3.118 ms for acquiring one image). B) Image of droplets with cell encapsulation at $\lambda = 0.7$. C) Image of droplets from the collection outlet after single-cell droplets sorting. D) Image of droplets from the collection outlet after multi-cell droplet sorting. Scale bar: 100 μm. E) Simulated possibility of the number of cells encapsulated in a droplet with different λ values from 0.1 to 0.9. F) Distribution of droplets containing different numbers of cells after single-cell droplet sorting. G) Distribution of droplets containing different numbers of cells after multi-cell droplet sorting.

increased to 97.9%, whereas the empty and multi-cell droplets decreased to 0.6% (rejecting ≈99%) and 1.5% (rejecting ≈90%), respectively (Figure 4C,F). According to the sorting result, the sorting accuracy (also purity, defined as the ratio of sorted target droplets and sorted droplets) of GL-IADS depends almost entirely on the recognition accuracy due to the reliable acoustofluidic deflection. For example, the accuracy of recognizing empty and cell-laden droplets was 100%, while the sorting accuracy of cell-laden reached 99.4%. In the droplet recognition assay, the loss rate of single-cell droplets is 5% when N in the same range of 140–190, which can basically represent the loss rate of single-cell droplets during sorting. In addition, the GL-IADS was also able to sort multi-cell droplets. Under the same experimental conditions, the image classification parameter N for multi-cell droplets was set to the range of <130. When the N of the detected droplet was below 130, the function generator turned on and lasted for 200 μs. The sorting process was as in Movie S2 (Supporting Information). After sorting, the multi-cell droplets increased to 97.4%, whereas the single-cell and empty droplets decreased to 2.3% and 0.3%, respectively (Figure 4D,G). Moreover, the size of the sorted droplets remained uniform (Figure 4C,D). This attributed to the fact that the setting radius threshold of Hough circle transform can only detect the droplets with diameter of 45 μm, the undetected droplet debris would not participate in acoustic sorting operation and flows into the waste outlet due to a low flow resistance, as shown in the Movie S3

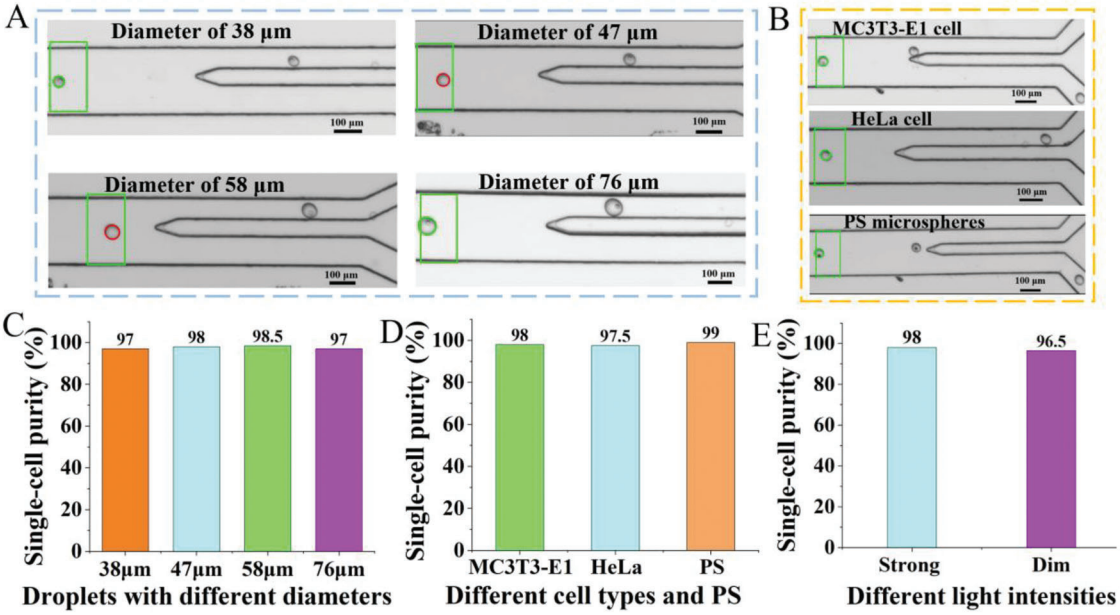

Figure 5. Applicability of GL-IADS. A) Recognizing and sorting single-cell droplets of varying sizes. B) Recognizing and sorting single-cell droplets for different cell types and PS microspheres. C) Single-cell sorting purities for droplets with different diameters. D) Single-cell sorting purities for different cell types. E) Robustness validation of single-cell sorting under different light intensities.

(Supporting Information). According to these results, the GL-IADS could achieve label-free, high-accuracy screening of single-cell, multi-cell or cell-laden droplets from high-concentration cells encapsulation while controlling the uniform size of droplets.

2.5. Applicability of GL-IADS in Sorting Droplets of Varying Sizes and Different Cell Types

Th GL-IADS adopted a Hough Circle Transform algorithm to identify microdroplets of varying sizes. In principle, this algorithm is based on the geometric characteristics of circles. As long as the droplets maintain a relatively circular shape, the algorithm can be adjusted to identify different diameters. To prove that the sorter is applicable to droplets within a wide size range, we conducted four groups of single-cell sorting experiments targeting droplets of different diameters (**Figure 5**A). For droplets with diameters of 38, 47, 58, and 76 μm, we set the radial detection parameter in the Hough Circle Transform algorithm to be 9–12, 13–15, 15–17, and 19–21 pixels, respectively. The GL-IADS accurately identified the droplets of all sizes without omission. Moreover, in the form of video recording, we analyzed 200 droplets sorted into the collection outlet for each group. For droplets with diameters of 38, 47, 58, and 76 μm, the single-cell sorting purities were 97%, 98%, 98.5%, and 97%, respectively (Figure 5C). A video (Movie S4, Supporting Information) visually showed that the GL-IADS accurately identified the four sizes of droplets and achieved single-cell sorting. The GL-IADS adopted gray-level recognition method to achieve droplet classification. Since cells can form a certain gray contrast with droplets, this sorter is suitable for sorting different types of cells. To verify this, we carried out the single-cell sorting of HeLa cells, MC3T3-E1 cells, and polystyrene (PS) microspheres (Figure 5B). In the form of video recording, we analyzed 200 droplets sorted into the collection channel for each group. For MC3T3-E1 cells, HeLa cells, and PS microspheres, the single-cell sorting purities were 98%, 97.5%, and 99%, respectively. The video (Movie S5, Supporting Information) visually showed that the GL-IADS accurately achieved single-cell sorting for different cell types. However, it is noteworthy that when sorting PS microspheres, we changed the droplet classification parameter. The gray threshold of 180 was changed to 90. The number of pixels with a gray value <90 ranging from 10–30 was judged as single-PS droplets. This is because PS microspheres exhibit a very dark color within droplets, and the number of pixels with a gray value <90 is 0 for empty droplets. In addition, to demonstrate the light intensity drift correction algorithm can effectively maintain the robustness of GL-IADS under varying lighting conditions. A single-cell sorting experiment under different light intensities was conducted. Also, in the form of video recording, we analyzed 200 droplets sorted into the collection channel for the two light intensities. For strong and dim light intensity, the single-cell sorting purities were 98% and 96.5% (Figure 5E), respectively. Movie S6 (Support Information) visually demonstrates that GL-IADS can accurately sort single-cell droplets regardless of relatively strong illumination or dim illumination. The GL-IADS is flexible and adaptable for various droplet sizes and different cell types, and is also robust under varying lighting conditions.

2.6. Post-sorting Cell Viability and Proliferation Analysis

The biocompatibility of the GL-IADS was confirmed experimentally. Unlabeled ADSCs were used for droplet generation and separation. Three cell groups of initial ADSCs (prepared for

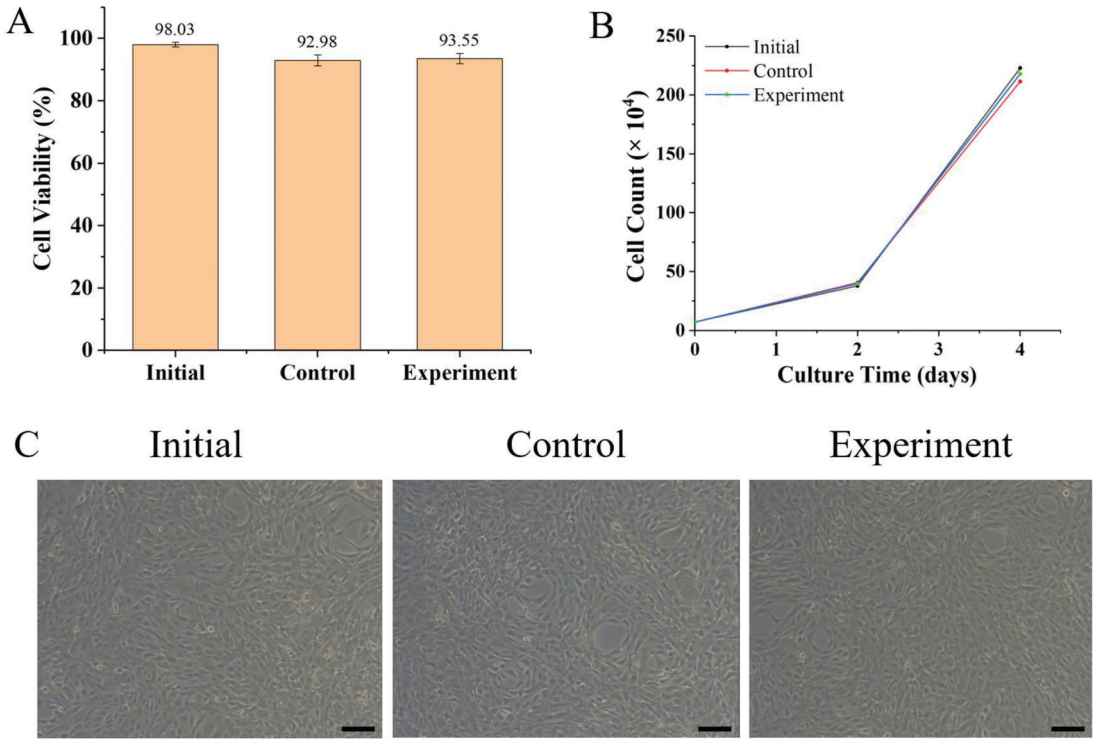

Figure 6. Viability and proliferation analysis of ADSCs after exposure to SSAW in GL-IADS. A) Viability of ADSCs described above, evaluated by trypan blue staining. B) Proliferation analysis of ADSCs by cell counting on days 2 and 4 after sorting and seeding. C) Image of ADSC confluence in the six-well plate on day 4. Scale bar: 100 μm.

experiment but not loaded into droplets), control ADSCs (loaded into droplets but not exposed to SSAW field), and experimental ADSCs (loaded into droplet and exposed to SSAW field) were analyzed for cell viability by trypan blue staining and their proliferation ability. **Figure** 6A shows the viability percentages of experimental and control groups were 93.5% and 92.9%, respectively, which decreased by ≈5% compared with that of initial ADSCs. Considering there almost no difference between the control and experimental groups, the decreased viability was probably caused by the toxic reagent of perfluorooctanol during the droplet demulsification process. The proliferation ability of cells was verified by counting cell number under the microscope. The three groups of ADSCs were seeded in cell culture-treated six-well plates with an initial number of 73 000 cells. The number of cells on days 2 and 4 were counted. As shown in Figure 6B, the three groups of ADSCs could proliferate normally, and almost no difference in the proliferation rate among them. On day 4, the three groups of ADSCs reached almost 100% confluence in the six-well plate (Figure 6C). The post-sorting biological analysis proved that the viability and proliferation of cells after exposure to SSAW field in the GL-IADS were not affected.

3. Discussion

The GL-IADS accuracy for cell-laden and single-cell droplets were >99% and 97.9%. That is, in a library containing 1 million of droplets to be screened, a 1% error rate means that only 10 000 droplets would be incorrectly sorted. In contrast, a sorter running at accuracy of 80% will result in 200 000 incorrect droplets, which is a very large number that could severely impact downstream analysis and even lead to erroneous conclusions. Thus, the high accuracy of GL-IADS could improve the efficiency of many biological assays that require encapsulating cells or even just one cell, such as cell-laden hydrogel for tissue engineering [28,50] and single-cell-based analysis.[51,52] In addition, the sorter could also enrich multi-cell droplets (accuracy of 97.4%), which can be further utilized in multicellular spheroid culture and sorting.[39]

The GL-IADS can high-accuracy recognize the droplets containing no cells, exactly one cell, and multiple cells, which enables the GL-IADS to sort single-cell droplets from a high-concentration cell encapsulation regardless of the probability of multi-cell droplets, ultimately increasing the sorting throughput and avoiding large dilution of the cell sample solution. Here, we achieved single-cell droplet sorting with the purity of 97.9% at a throughput of 43 Hz, from a cell encapsulation ($\lambda = 0.7$) with a single-cell and multi-cell droplet ratio of 34.7% and 15.5%. In contrast, to achieve single-cell sorting with a purity of 97.5%, the technologies that cannot recognize multi-cell droplets need to adopt high-diluted cell encapsulation ($\lambda = 0.05$) with a single-cell and multi-cell droplet ratio of 4.76% and 0.12% (according to Poisson distribution).[36] This is still under the consideration that it can completely reject empty droplets, otherwise, λ needs to be further reduced. Comparing the actual throughput, the GL-IADS can enrich 53.7 k single-cell droplets in 1 h, which is equivalent to the throughput of 313 Hz of those that cannot recognize multi-cell droplets. In addition, a heavily diluted cell suspension of generates mostly empty droplets that encapsulated waste reagent,

brings cost issues to expensive applications such as single-cell RNA sequencing,[36,39] which could be solved and avoided by the GL-IADS.

The gray-level recognition method shortens the image processing time to ≈300 µs while ensuring the sorting accuracy of single-cell, multi-cell, and cell-laden droplets >97%. Moreover, it does not require a high-performance computing computer and advanced imaging hardware. To achieve this droplet classification, the image processing time of machine learning-IADS exceeds 14 ms (Table S1, Supporting Information), which limited their sorting throughput. The current GL-IADS throughput of 43 Hz was chosen based on the maximum frame rate (320 fps) of CMOS camera and the latency time (12 ms) of function generator to ensure accurate sorting of single-cell droplets. When adopting a fast-response function generator that commonly used in SAW-based FADS[23,37] and a high-speed camera such as >2000 fps, the GL-IADS make it possible to achieve label-free, high-accuracy single-cell droplet sorting with an ultra-high throughput up to hundreds or even KHz. By then, the sorter will have the potential to revolutionize single-cell researches.

Highly monodispersed droplets are required for many applications such as cell toxicity screening, antibody discovery, and drug screening. The presence of polydisperse droplets could cause them containing inconsistent amounts of biological reagents. However, the occasional unintentional droplet merging (resulting in larger droplet) and splitting (resulting in smaller droplet debris) are unavoidable even in the advanced sorting operation.[53] The conventional droplet sorters are based on the droplet parameters such as fluorescent or impedance signals. In absence of the droplet size information, incorrectly sized droplets can be easily classified as target object.[36] Our GL-IADS adopted a Hough circle transform algorithm to achieve target-size droplet detection. By narrowing the parameter range of circular radius detection, the sorter enables the sorted droplets to maintain a uniform size. For example, the setting circle radius parameter of 13.5–14.5 pixels can high-accuracy detect the target-size droplets (diameter of 45 µm) without omission. The merged droplets and droplet debris, whether they contain cell or not, cannot be detected due to its obvious size difference with the target-size droplets. The unrecognized droplets cannot participate in the acoustic sorting operation and automatically flow into the waste outlet. However, although the sorted droplets remain uniform size in this work, the number of droplet debris or merged droplet is ultimately small compared to the target droplets. In subsequent works, the specific experiments containing highly-polydisperse droplets should be designed to further explore and improve the size control capability of the sorter, such as the trade-off between size accuracy and droplet miss rate, the space control of droplet debris with target droplets, thus meeting the requirements of applications that are prone to encounter droplet size uniformity issues.

The GL-IADS is flexible and adaptable. Table S1 (Supporting Information) summarizes the comparison of some key parameters between GL-IADS and other sorting technologies. The GL-IADS adopted a Hough circle transform algorithm to achieve target-size droplet identification. There is no need to rely on a specific flow channel structure or resort to other technologies. By properly adjust the circle radius parameter, the sorter is applicable to sorting droplets of varying diameters and ensure the size uniformity of sorted droplets. The GL-IADS achieved droplet classification (empty, single-cell, and multi-cell) based on a gray recognition method, which is also applicable to different cell types. Although the optical properties of different cells may differ slightly, cells are generally visible inside the droplets and have a certain gray contrast with the droplets. For our GL-IADS, the more obvious the gray contrast, the easier it is to achieve droplet classification. However, even when the grayscale contrast between the cells and the droplets was relatively small, such as under very dim lighting conditions, we were still able to achieve accurate single-cell sorting. Additionally, the GL-IADS also demonstrated strong robustness under varying lighting conditions.

4. Conclusion

In summary, the GL-IADS integrates a gray-level-based image recognition method with a reliable acoustofluidic actuation system, achieving label-free, high-accuracy screening of single-cell, multi-cell, and cell-laden droplets. Recognition and rejection multi-cell droplets overcome the tradeoff between throughput and purity for single-cell droplet sorting in previous droplet sorters. Even in the high-concentration cell encapsulation (λ = 0.7), the purity of GL-IADS sorting single-cell droplets still reaches 97.9% with a throughput of 43 Hz, by rejecting ≈99% empty and ≈90% multi-cell droplets. Moreover, the sorter reduces the image processing time to ≈300 µs, which offers promise to achieve label-free single-cell droplets sorting at ultra-high throughput up to KHz. The sorter is also applicable to droplets of varying size and ensures the monodispersity of the sorted droplets by rejecting merged droplets and/or droplet debris. In addition, the sorter demonstrated high biocompatibility by cell viability and proliferation assay. The GL-IADS can be integrated into a broad range of droplet microfluidics-based screening applications.

5. Experimental Section

Detachable Acoustofluidic Chip Fabrication: The detachable acoustofluidic chip consists of a SAW transducer and a disposable PDMS channel. The SAW transducer has a set of 16 pairs of U-FIDTs with a finger feature size of 33 µm and a wavelength of 396 µm, corresponding to a resonance frequency of 10 MHz. The arc angle and innermost radius of the U-FIDTs were 20° and 600 µm, respectively. To fabricate the SAW transducer, the photoresist of AZ5214 (Clariant, USA) was patterned on a 1 mm thick Y-128° cut $LiNbO_3$ substrate via standard lithography, on which then the metal layers (Cr/Au, 10/100 nm) were then deposited by magnetron sputtering. After a lift-off process, the U-FIDTs were obtained. The disposable PDMS channel was obtained by bonding the PDMS channel to a PDMS film with a 20 µm thickness. The PDMS channel was fabricated by standard soft-lithography (Figure S3A–D, Supporting Information). In brief, a 50 µm thick microchannel mold was fabricated on a silicon wafer using SU8-2050 photoresist (MicroChem, USA) by photolithography. PDMS was mixed with the curing agent (Sylgard 184 Elastomer Kit, Dow Corning Corp, USA) at a ratio of 10:1 and then poured into the microchannel mold. After being baked in an 80 °C oven for 2 h, the cured PDMS channel was peeled from the microchannel mold and punched with 1 mm through-holes in inlet and outlet positions. Two square cavities are symmetrically distributed on both sides of the sorting channel of the PDMS channel, which was used for the formation of micropillars. The PDMS channel and a PDMS film were permanently bonded after oxygen plasma (PDC-002-HP, Harrick plasma, USA) treatment and baked in an 80 °C oven for 1 h

to form the disposable PDMS channel (Figure S3E,F, Supporting Information). Then, the micropillar with a width of 660 µm was obtained by using a knife to cut off the PDMS film piece under two symmetrical cavities (Figure S3G, Supporting Information). The process of cutting of the PDMS film piece can be easily completed manually, because this piece did not touch the top PDMS during the bonding process. Finally, the detachable acoustofluidic chip was assembled by hand-placing the disposable PDMS channel on the SAW transducer with alignment under the microscope (Figure S3H, Supporting Information). After each test, the disposable PDMS channel was peeled and discarded, while the SAW transducer could be recycled for next use.

Cell Culture and Harvesting: Human adipose-derived mesenchymal stem cells (ADSCs) were cultured in Iscove's Modified Dulbecco's medium (IMDM) (12440053, Gibco, USA) containing 10% fetal bovine serum (10270106, Gibco, USA) supplemented with 1% antibiotic-antimycotic (15 240096, Gibco, USA) and 10 ng mL^{-1} FGF2 (100-18B, PeproTech, USA) at 37 °C in 5% CO_2. The MC3T3-E1 cells and HeLa cells were maintained in Dulbecco's minimum essential medium (DMEM) (11965092, Gibco, USA) supplemented with 10% fetal bovine serum (FBS; 10270106, Gibco, USA), penicillin (100 U mL^{-1}), and streptomycin (100 U mL^{-1}; 15240062, Invitrogen, USA) at 37 °C in 5% CO_2. The ADSCs, MC3T3-E1, and HeLa cells were detached using the 1X of trypsin-EDTA (15090046, Gibco, USA) when reaching ≈80% confluency in a 100 mm cell culture dish (CS016-0128, ExCell Bio, China), centrifuged at 300 g for 3 min. The ADSCs, MC3T3-E1, and HeLa cells were resuspended in IMDM to prepare for droplet generation.

Random Cell Encapsulation in Droplets: The water in oil droplets were generated in an independent flow-focusing microfluidics chip.[54] A cell solution and HFE-7500 oil were kept in two syringes, which connect the internal injection port and the peripheral injection port of this chip via polyethylene tubing (0.38 mm ID × 1.09 mm OD; 427 406, BD Intramedic, USA). The two syringes were pushed by the syringe pump (TS-1B, Longer Pump, England). Under this experimental condition, monodispersed droplets were stably generated and collected to prepare for target droplet sorting.

Experimental Setup: The detachable acoustofluidic chip was placed on the stage of an upright microscope (Nikon Corporation, Japan) with a 4 × objective, to which a Hamamatsu CMOS camera (C134440-20CU, Hamamatsu, Japan) was connected. The droplets were kept in a storage syringe, and HFE-7500 oil was injected into the inner and peripheral inlet of the acoustofluidic chip at a flow speed of 10 and 360 µL/30 min, respectively. The moving droplets in the sorting channel were imaged and acquired in real time by the CMOS camera. The acquired microscopic images were 8-bit grayscale images. The field of view of the microscopic image was 1024 × 256 pixels, the field of view of the ROI was 150 × 80 pixels, the acquisition speed was 320 fps, and the exposure time was set to 10 µs. These images were processed frame by frame for droplet detection, classification, and decision-making by the image processing system. The image processing system consists of a debugging program and a sorting program, which were written in C++ by using the computer vision library OpenCV. The debugging program outputted the corresponding picture and a text file containing pixel information for every detected droplet, which was for data statistics and parameter correction. However, the large number of high-definition pictures could cause the computer's CPU to be fully loaded and run for only a few minutes only. The sorting program was the same as the debugging program except that it does not output pictures and text files, which could keep running for droplet sorting smoothly. Therefore, the sorting program adopted the correction parameters of the debugging program to conduct sorting experiments. Calculations were performed on a desktop computer (DELL, Windows 10, 64-bit operating system with an Intel i5-12500 3.0 GHz processor with 8192 MB RAM). When a target droplet was detected, the image processing system gave the function generator (DG4162, Rigol, China) a turn-on sine wave command of 9.73 MHz frequency and 0.8 Vpp voltage. The sinewave was amplified by a factor of 32 dB with a power amplifier (RF-UWB-10M1G-8 W, China) to make the voltage reach 32 Vpp, which was then split to two signals and applied to two identical U-FIDTs to generate SSAW for droplet deflection.

Cell Viability and Proliferation Assay: The initial ADSCs were suspended in 1 mL of fresh medium in 1.5 mL tube at room-temperature. The control ADSCs and experimental ADSCs were recovered through a droplet rupture process as follows. First, 300 µL of 20% 1H, 1H, 2H, 2H-perfluorooctanol (AAB2015609, Thermo Scientific, USA) was added into the droplet collection tube and gently vortexed for 1 min for the droplets to merge into a bulk solution. Second, the upper bulk solution was transferred to a new tube and centrifuged at 300 g for 5 min to collect the cells. The collected control and experimental ADSCs were then resuspended in 1 mL of fresh medium in 1.5 mL tube. Afterward, the cell viability of the three groups was analyzed by trypan blue staining (ST2780, Beyotime, China) and microscopic observation. Proliferation assay was conducted in the cells. The three groups of ADSCs were seeded in cell culture-treated six-well plates with an initial number of 73 000 cells. Then, the number of cells on days 2 and 4 were counted by a hemocytometer (Marienfeld Superior, Marienfeld, Germany) under a microscope (Axio Vert.A1, Germany) with a camera (Axiocam 105 color, Germany).

Supporting Information

Supporting Information is available from the Wiley Online Library or from the author.

Acknowledgements

Z.L. and Y.Z. contributed equally to this work. This work was supported by grants from the Research Grants Council of the Hong Kong Special Administrative Region, China (Project No. CityU C1134-20G and CityU 11211421), Shenzhen Science and Technology Innovation Commission, China (Project No. SGDX2020110309300502), and the National Natural Science Foundation of China (62333012).

Conflict of Interest

The authors declare no conflict of interest

Data Availability Statement

The data that support the findings of this study are available from the corresponding author upon reasonable request.

Keywords

acoustofluidic, droplet microfluidics, image-activated droplet sorting, single-cell encapsulation

Received: January 14, 2025
Revised: April 3, 2025
Published online: May 8, 2025

[1] E. Z. Macosko, A. Basu, R. Satija, J. Nemesh, K. Shekhar, M. Goldman, I. Tirosh, A. R. Bialas, N. Kamitaki, E. M. Martersteck, J. J. Trombetta, D. A. Weitz, J. R. Sanes, A. K. Shalek, A. Regev, S. A. McCarroll, *Cell* **2015**, *161*, 1202.
[2] J. Bues, M. Biočanin, J. Pezoldt, R. Dainese, A. Chrisnandy, S. Rezakhani, W. Saelens, V. Gardeux, R. Gupta, R. Sarkis, J. Russeil, Y. Saeys, E. Amstad, M. Claassen, M. P. Lutolf, B. Deplancke, *Nat. Methods* **2022**, *19*, 323.
[3] A. A. Nawaz, M. Urbanska, M. Herbig, M. Nötzel, M. Kräter, P. Rosendahl, C. Herold, N. Toepfner, M. Kubánková, R. Goswami, S. Abuhattum, F. Reichel, P. Müller, A. Taubenberger, S. Girardo, A. Jacobi, J. Guck, *Nat. Methods* **2020**, *17*, 595.

[4] X. Xu, J. Wang, L. Wu, J. Guo, Y. Song, T. Tian, W. Wang, Z. Zhu, C. Yang, *Small* **2020**, *16*, 1903905.
[5] D. Liu, M. Sun, J. Zhang, R. Hu, W. Fu, T. Xuanyuan, W. Liu, *Analyst* **2022**, *147*, 2294.
[6] Z. Jiang, H. Shi, X. Tang, J. Qin, *TrAC – Trends Anal. Chem.* **2023**, *159*, 116932.
[7] D. Gao, F. Jin, M. Zhou, Y. Jiang, *Analyst* **2019**, *144*, 766.
[8] M. Li, H. Liu, S. Zhuang, K. Goda, *RSC Adv.* **2021**, *11*, 20944.
[9] T. Woyke, D. F. R. Doud, F. Schulz, *Nat. Methods* **2017**, *14*, 1045.
[10] N. Nitta, T. Sugimura, A. Isozaki, H. Mikami, K. Hiraki, S. Sakuma, T. Iino, F. Arai, T. Endo, Y. Fujiwaki, H. Fukuzawa, M. Hase, T. Hayakawa, K. Hiramatsu, Y. Hoshino, M. Inaba, T. Ito, H. Karakawa, Y. Kasai, K. Koizumi, S. W. Lee, C. Lei, M. Li, T. Maeno, S. Matsusaka, D. Murakami, A. Nakagawa, Y. Oguchi, M. Oikawa, T. Ota, et al., *Cell* **2018**, *175*, 266.
[11] Z. Dong, H. F. Wang, J. B. Chen, Q. Fang, *Sensors Actuators B Chem.* **2025**, *426*, 136993.
[12] A. Isozaki, Y. Nakagawa, M. H. Loo, Y. Shibata, N. Tanaka, D. L. Setyaningrum, *Sci. Adv.* **2020**, *6*, aba6712.
[13] S. Müller, G. Nebe-Von-Caron, *FEMS Microbiol. Rev.* **2010**, *34*, 554.
[14] W. Verbist, J. Breukers, S. Sharma, I. Rutten, H. Gerstmans, L. Coelmont, F. Dal Dosso, K. Dallmeier, J. Lammertyn, *Lab Chip* **2024**, *24*, 2107.
[15] Y. Feng, Z. Cheng, H. Chai, W. He, L. Huang, W. Wang, *Lab Chip* **2022**, *22*, 240.
[16] K. Lee, S. E. Kim, J. Doh, K. Kim, W. K. Chung, *Lab Chip* **2021**, *21*, 1798.
[17] T. Luo, L. Fan, R. Zhu, D. Sun, *Micromachines* **2019**, *10*, 104.
[18] Y. Wang, Y. Xue, X. Hong, H. Wang, C. Zhou, W. Wang, J. Sheng, P. Liang, H. Li, Q. Xu, Y. Wang, K. Liu, L. Shang, H. Peng, F. Chen, K. Zhang, H. Yin, Y. Wang, F. Deng, S. Feng, W. E. Huang, B. Li, *Sensors Actuators B Chem.* **2025**, *427*, 137202.
[19] Y. Wang, Y. Xue, H. Wang, Y. Qu, K. Zhang, L. Shang, P. Liang, F. Chen, X. Tang, W. Luo, L. K. Chin, S. Feng, B. Li, *ACS Sens.* **2025**, *10*, 846.
[20] J. De Jonghe, T. S. Kaminski, D. B. Morse, M. Tabaka, A. L. Ellermann, T. N. Kohler, G. Amadei, C. E. Handford, G. M. Findlay, M. Zernicka-Goetz, S. A. Teichmann, F. Hollfelder, *Nat. Commun.* **2023**, *14*, 4788.
[21] H. S. Moon, K. Je, J. W. Min, D. Park, K. Y. Han, S. H. Shin, W. Y. Park, C. E. Yoo, S. H. Kim, *Lab Chip* **2018**, *18*, 775.
[22] O. J. Miller, A. El Harrak, T. Mangeat, J. C. Baret, L. Frenz, B. El Debs, E. Mayot, M. L. Samuels, E. K. Rooney, P. Dieu, M. Galvan, D. R. Link, A. D. Griffiths, *Proc. Natl. Acad. Sci.* **2012**, *109*, 378.
[23] R. Zhong, S. Yang, G. S. Ugolini, T. Naquin, J. Zhang, K. Yang, J. Xia, T. Konry, T. J. Huang, *Small* **2021**, *17*, 2103848.
[24] C. Sun, L. Liu, L. Pérez, X. Li, Y. Liu, P. Xu, E. A. Boritz, J. I. Mullins, A. R. Abate, *Nat. Biomed. Eng.* **2022**, *6*, 1004.
[25] M. Boutros, F. Heigwer, C. Laufer, *Cell* **2015**, *163*, 1314.
[26] T. Tang, H. Zhao, S. Shen, L. Yang, C. T. Lim, *Microsystems Nanoeng.* **2024**, *10*, 3.
[27] E. W. M. Kemna, R. M. Schoeman, F. Wolbers, I. Vermes, D. A. Weitz, A. Van Den Berg, *Lab Chip* **2012**, *12*, 2881.
[28] A. M. White, Y. Zhang, J. G. Shamul, J. Xu, E. A. Kwizera, B. Jiang, X. He, *Small* **2021**, *17*, 2100491.
[29] G. Sun, L. Qu, F. Azi, Y. Liu, J. Li, X. Lv, G. Du, J. Chen, C. H. Chen, L. Liu, *Biosens. Bioelectron.* **2023**, *225*, 115107.
[30] J. Jiang, G. Yang, F. Ma, *Biotechnol. Adv.* **2023**, *66*, 108173.
[31] M. Pires-Santos, S. Nadine, J. F. Mano, *Small Sci.* **2024**, *4*, 2300332.
[32] E. C. Jensen, *Anat. Rec.* **2012**, *295*, 2031.
[33] N. Nitta, T. Iino, A. Isozaki, M. Yamagishi, Y. Kitahama, S. Sakuma, Y. Suzuki, H. Tezuka, M. Oikawa, F. Arai, T. Asai, D. Deng, H. Fukuzawa, M. Hase, T. Hasunuma, T. Hayakawa, K. Hiraki, K. Hiramatsu, Y. Hoshino, M. Inaba, Y. Inoue, T. Ito, M. Kajikawa, H. Karakawa, Y. Kasai, Y. Kato, H. Kobayashi, C. Lei, S. Matsusaka, H. Mikami, et al., *Nat. Commun.* **2020**, *11*, 3452.
[34] H. Liu, L. Nan, F. Chen, Y. Zhao, Y. Zhao, *Lab Chip* **2023**, *23*, 2497.
[35] Y. Gu, A. C. Zhang, Y. Han, J. Li, C. Chen, Y. H. Lo, *Cytom. Part A* **2019**, *95*, 499.
[36] J. Zhong, M. Liang, Q. Tang, Y. Ai, *Mater. Today Bio.* **2023**, *19*, 100594.
[37] P. Li, Z. Ma, Y. Zhou, D. J. Collins, Z. Wang, Y. Ai, *Anal. Chem.* **2019**, *91*, 9970.
[38] A. Chu, D. Nguyen, S. S. Talathi, A. C. Wilson, C. Ye, W. L. Smith, A. D. Kaplan, E. B. Duoss, J. K. Stolaroff, B. Giera, *Lab Chip* **2019**, *19*, 1808.
[39] V. Anagnostidis, B. Sherlock, J. Metz, P. Mair, F. Hollfelder, F. Gielen, *Lab Chip* **2020**, *20*, 889.
[40] M. Girault, H. Kim, H. Arakawa, K. Matsuura, M. Odaka, A. Hattori, H. Terazono, K. Yasuda, *Sci. Rep.* **2017**, *7*, 40072.
[41] L. Howell, V. Anagnostidis, F. Gielen, *Adv. Mater. Technol.* **2022**, *7*, 2101053.
[42] Q. Liu, K. Guo, L. Jiang, H. Yang, Z. Ni, N. Xiang, *Sensors Actuators B Chem.* **2024**, *419*, 136408.
[43] C. Frey, J. Pfeil, T. Neckernuss, D. Geiger, K. Weishaupt, I. Platzman, O. Marti, J. P. Spatz, *View* **2020**, *1*, 20200101.
[44] M. Durve, S. Orsini, A. Tiribocchi, A. Montessori, J. M. Tucny, M. Lauricella, A. Camposeo, D. Pisignano, S. Succi, *Eur. Phys. J. E* **2023**, *46*, 32.
[45] S. Zhao, M. Wu, S. Yang, Y. Wu, Y. Gu, C. Chen, J. Ye, Z. Xie, Z. Tian, H. Bachman, P. H. Huang, J. Xia, P. Zhang, H. Zhang, T. J. Huang, *Lab Chip* **2020**, *20*, 1298.
[46] J. Shi, H. Huang, Z. Stratton, Y. Huang, T. J. Huang, *Lab Chip* **2009**, *9*, 3354.
[47] M. Wu, Z. Mao, K. Chen, H. Bachman, Y. Chen, J. Rufo, L. Ren, P. Li, L. Wang, T. J. Huang, *Adv. Funct. Mater.* **2017**, *27*, 1606039.
[48] Z. Ma, D. J. Collins, Y. Ai, *Anal. Chem.* **2016**, *88*, 5316.
[49] J. Park, J. H. Jung, K. Park, G. Destgeer, H. Ahmed, R. Ahmad, H. J. Sung, *Lab Chip* **2018**, *18*, 422.
[50] X. He, *ACS Biomater. Sci. Eng.* **2017**, *3*, 2692.
[51] F. Ahmadi, H. Tran, N. Letourneau, S. R. Little, A. Fortin, A. N. Moraitis, S. C. C. Shih, *Small* **2024**, *20*, 2308950.
[52] W. min Zhou, Y. yan Yan, Q. ru Guo, H. Ji, H. Wang, T. tian Xu, B. Makabel, C. Pilarsky, G. He, X. yong Yu, J. ye Zhang, *J. Nanobiotechnol.* **2021**, *19*, 1.
[53] H. Zhang, R. Gupte, Y. Li, C. Huang, A. R. Guzman, J. J. Han, H. Jung, R. Sabnis, P. de Figueiredo, A. Han, *Nat. Commun.* **2024**, *15*, 9444.
[54] J. Sun, H. T. Jessica Lo, L. Fan, T. L. Yiu, A. Shakoor, G. Li, W. Y. W. Lee, D. Sun, *Sci. Adv.* **2022**, *8*, abp9245.